Commun. Comput. Phys.
doi: 10.4208/cicp.020810.171210a

Vol. **10**, No. 5, pp. 1184-1210
November 2011

Numerical Methods for Balance Laws with Space Dependent Flux: Application to Radiotherapy Dose Calculation

Christophe Berthon[1], Martin Frank[2,*], Céline Sarazin[1] and Rodolphe Turpault[1]

[1] *Université de Nantes, Laboratoire de Mathématiques Jean Leray, UMR6629, 2 rue de la Houssinière, BP 92208, 44322 Nantes Cedex 3, France.*
[2] *RWTH Aachen University, Mathematics, Center for Computational Engineering Science, Schinkelstrasse 2, 52062 Aachen, Germany.*

Received 2 August 2010; Accepted (in revised version) 17 December 2010

Communicated by Kazuo Aoki

Available online 2 August 2011

Abstract. The present work is concerned with the derivation of numerical methods to approximate the radiation dose in external beam radiotherapy. To address this issue, we consider a moment approximation of radiative transfer, closed by an entropy minimization principle. The model under consideration is governed by a system of hyperbolic equations in conservation form supplemented by source terms. The main difficulty coming from the numerical approximation of this system is an explicit space dependence in the flux function. Indeed, this dependence will be seen to be stiff and specific numerical strategies must be derived in order to obtain the needed accuracy. A first approach is developed considering the 1D case, where a judicious change of variables allows to eliminate the space dependence in the flux function. This is not possible in multi-D. We therefore reinterpret the 1D scheme as a scheme on two meshes, and generalize this to 2D by alternating transformations between separate meshes. We call this procedure projection method. Several numerical experiments, coming from medical physics, illustrate the potential applicability of the developed method.

AMS subject classifications: 35L65, 65N08, 92C99

Key words: Radiotherapy, hyperbolic system of conservation laws, source term approximations, finite volume methods.

*Corresponding author. *Email addresses:* christophe.berthon@math.univ-nantes.fr (C. Berthon), frank@ mathcces.rwth-aachen.de (M. Frank), celine.sarazin@univ-nantes.fr (C. Sarazin), rodolphe.turpault@univ-nantes.fr (R. Turpault)

 ©2011 Global-Science Press

1 Introduction

This paper is concerned with the numerical approximation of the set of balance laws

$$\partial_\varepsilon \Psi^0(\mathbf{x},\varepsilon) - \nabla_x \cdot \Big(\frac{1}{\rho(\mathbf{x})} \mathbf{\Psi}^1(\mathbf{x},\varepsilon) \Big) = 0, \tag{1.1a}$$

$$\partial_\varepsilon \mathbf{\Psi}^1(\mathbf{x},\varepsilon) - \nabla_x \Big(\frac{1}{\rho(\mathbf{x})} D_e \Big(\frac{\mathbf{\Psi}^1(\mathbf{x},\varepsilon)}{\Psi^0(\mathbf{x},\varepsilon)} \Big) \Psi^0(\mathbf{x},\varepsilon) \Big) = T(\mathbf{x},\varepsilon) \mathbf{\Psi}^1(\mathbf{x},\varepsilon). \tag{1.1b}$$

As will be explained below, this system describes charged particle transport in tissue, and can be used as a novel method for dose calculation in radiotherapy. The particular challenge in the numerical approximation of this system of hyperbolic balance laws is that the flux function depends explicitly on a density $\rho(\mathbf{x})$. In addition, this density can vary over several orders of magnitude, from $\rho \sim 1$ (water) to $\rho \sim 10^{-3}$ (air). A standard discretization would therefore require a very small time step, which would make the computations infeasible. To overcome this problem, we develop a specific technique to deal with the strongly varying space-dependent flux. Several authors have worked on analysis and numerical methods for conservation laws for discontinuous flux. An overview can be found in the recent paper [45]. Our approach is new because it uses the specific structure of the discontinuous coefficient and introduces a method that is based on variable transformations.

Radiotherapy is the treatment of cancer and other diseases with a certain type of ionizing radiation. This radiation deposits energy that injures or destroys cells in the area being treated, by damaging their genetic material. Indeed, the incoming particles ionize atoms and make the cells unstable. Physicians want to determine the best beam setup to destroy the tumor while minimizing the damage to healthy tissue. To that end, one needs to predict and visualize the radiation dose in the patient's body before the treatment. The data used, which usually comes from a CT (Computer Tomography) scan, consist of 2D slices describing the density of the tissues.

Up to now many clinical dose calculation algorithms rely on semi-empirical models. They are based on explicit solutions to radiation problems in a very simplified geometry (e.g., the one-dimensional Fermi-Eyges theory [18]). These explicit solutions are then combined with experimental data to compute the central-axis dose (e.g., [26]). Although many improvements of Fermi-Eyges theory were performed, e.g., by including additional correction factors [1, 27, 28, 37], they still produce errors of up to 12% near inhomogeneities [29].

Currently, statistical Monte-Carlo simulation codes are entering clinical practice [14, 38, 39]. These perform direct simulations of individual particle tracks which result from a random sequence of free flights and interaction events. In this way random histories are generated. If their number is large enough macroscopic quantities can be obtained by averaging over the simulated histories [2]. Monte Carlo tools model physical processes very precisely and can handle arbitrary geometries without losing accuracy. Although

they rank among the most accurate methods for predicting absorbed dose distributions, their high computation times have so far limited their use in clinics.

A different approach in the solution of radiation transport problems are deterministic calculations solving the linear Boltzmann transport equation. In principle, its solution will give very accurate dose distributions comparable to Monte Carlo simulations. Börgers [9] argued that under certain accuracy conditions deterministic methods could compete with Monte Carlo calculations. Recently, 3D dose calculations for real clinical test cases were performed with Attila [44]. Results with similar accuracy as Monte Carlo calculations were achieved in promising computation times. A finite-element discretization of the transport equation was proposed in [8].

This paper is a continuation of the work presented in [16] and [17]. A simple finite volume discretization is investigated in [16], where an unsteady version of the system (1.1) is considered. However, that scheme has a very strong restriction on the time step (due to the CFL condition) for small densities. Indeed, in real life radiotherapy experiments, the density of the matter can have large fluctuations and/or discontinuities. Air cavities have a density ρ, which is three orders of magnitude smaller than that of water. As a consequence, we have to derive suitable finite volume methods able to deal with large variations or discontinuities of the density. In addition, the proposed scheme will be cheaper than the finite volume method introduced in [16].

We assume that particle transport is governed by the following moment model:

$$\partial_\varepsilon\big(S_M(\mathbf{x},\varepsilon)\Psi^0(\mathbf{x},\varepsilon)\big)-\nabla_x\cdot\boldsymbol{\Psi}^1(\mathbf{x},\varepsilon)=0, \tag{1.2a}$$

$$\partial_\varepsilon\big(S_M(\mathbf{x},\varepsilon)\boldsymbol{\Psi}^1(\mathbf{x},\varepsilon)\big)-\nabla_x\boldsymbol{\Psi}^2(\mathbf{x},\varepsilon)=T_{tot}(\mathbf{x},\varepsilon)\boldsymbol{\Psi}^1(\mathbf{x},\varepsilon), \tag{1.2b}$$

where Ψ^0 is a positive scalar and $\boldsymbol{\Psi}^1$ belongs to $\mathbb{R}^d$, with d the space dimension. Here, the variable $\varepsilon>0$ describes the energy of the particle, while $\mathbf{x}\in\mathbb{R}^d$ is the space variable. Concerning $\boldsymbol{\Psi}^2$, an additional hypothesis will be imposed later-on to close the system. This model has been introduced in [20] and investigated further in [17].

The positive functions $S_M(\mathbf{x},\varepsilon)$ and $T_{tot}(\mathbf{x},\varepsilon)$, respectively called stopping power and transport coefficient, are determined by the type of particles and the type of the medium. The stopping power represents the energy loss of a particle per unit path length and the transport coefficient describes angular deviations which are mainly due to elastic scattering. From now on, let us emphasize a useful rewriting of S_M and T_{tot} as a product of the density of the matter $\rho(\mathbf{x})$ and a function of the energy:

$$S_M(\mathbf{x},\varepsilon)=\rho(\mathbf{x})S(\varepsilon)\quad\text{and}\quad T_{tot}(\mathbf{x},\varepsilon)=\rho(\mathbf{x})T(\varepsilon). \tag{1.3}$$

Here we have assumed that the tissue can be described as water with varying density. This is a good first approximation, and in the absence of more information on the CT scan the only viable assumption. Precise definitions of the functions $S(\varepsilon)$ and $\rho(\mathbf{x})$ will be given later on, according to the performed numerical experiments. However, let us note from now on, that these positive functions, $S(\varepsilon)$ and $\rho(\mathbf{x})$ are bounded from below

and from above by positive constants. In fact, this boundedness property will be useful to introduce several integral definitions needed in the sequel.

This model can be derived from an underlying kinetic equation of the form

$$-\partial_\varepsilon\big(S_M(\mathbf{x},\varepsilon)\Psi(\mathbf{x},\varepsilon,\mathbf{\Omega})\big)+\mathbf{\Omega}\cdot\nabla\Psi(\mathbf{x},\varepsilon,\mathbf{\Omega})=\int_{S^2}\sigma(\varepsilon,\mathbf{\Omega}\cdot\mathbf{\Omega}')\psi(\mathbf{x},\varepsilon,\mathbf{\Omega}')d\mathbf{\Omega}-\sigma_{tot}(\varepsilon')\psi(\mathbf{x},\varepsilon,\mathbf{\Omega}).$$

The unknown Ψ is the particle density in phase space, measured in units of particles per time, area, solid angle $\mathbf{\Omega}$ and energy ε normal to rays. The unknowns $\Psi^0,\mathbf{\Psi}^1$ in the M1 model are

$$\Psi^0(\mathbf{x},\varepsilon)=\int_{S^2}\Psi(\mathbf{x},\varepsilon,\mathbf{\Omega})d\mathbf{\Omega}\quad\text{and}\quad\mathbf{\Psi}^1(\mathbf{x},\varepsilon)=\int_{S^2}\mathbf{\Omega}\Psi(\mathbf{x},\varepsilon,\mathbf{\Omega})d\mathbf{\Omega}.$$

They are the total particle number and the particle flux (measured in units of particles per time, area, and energy normal to rays. Since they are the first two moments of a positive distribution function they must belong to the following admissible state space:

$$\mathcal{A}_d=\Big\{{}^t(\Psi^0,\mathbf{\Psi}^1)\in\mathbb{R}^{d+1},\ \Psi^0>0,\ \frac{\|\mathbf{\Psi}^1\|}{\Psi^0}<1\Big\},\tag{1.4}$$

where the mapping $\|\cdot\|$ denotes the usual Euclidean norm. After the work by Grad [24], devoted to rarefied gases, moment models as (1.2) are relevant alternatives to a kinetic description of microscopic phenomena.

The variable of interest in radiotherapy, the dose

$$D(\mathbf{x})=\int_0^\infty S(\varepsilon)\Psi^0(\mathbf{x},\varepsilon)d\varepsilon,\tag{1.5}$$

describes the energy deposited in the matter.

Since the dose is a macroscopic quantity, and we only need Ψ^0 to compute it, we are interested in a model that describes macroscopic quantities only. This model can be obtained by multiplying the kinetic equation with 1 and $\mathbf{\Omega}$ and integrating over $\mathbf{\Omega}$. This gives an underdetermined system. In order to complete the system, we have to give a closure law for Ψ^2. We adopt the entropy minimization strategy [32, 34] from [15] for radiative transfer (see also [19, 33, 35, 41, 42] for details and extensions).

The closed system, the so-called M1 model, reads:

$$\partial_\varepsilon(\rho S\Psi^0)-\nabla\cdot\mathbf{\Psi}^1=0,\qquad\partial_\varepsilon(\rho S\mathbf{\Psi}^1)-\nabla\cdot D_e\Big(\frac{\mathbf{\Psi}^1}{\Psi^0}\Big)\Psi^0=\rho T\mathbf{\Psi}^1,\tag{1.6}$$

where the Eddington tensor D_e is defined by:

$$D_e(f)=\frac{1-\chi(f)}{2}I_d+\frac{3\chi(f)-1}{2}\frac{f}{\|f\|}\otimes\frac{f}{\|f\|},\tag{1.7}$$

and where $f=\mathbf{\Psi}^1/\Psi^0$, for all ${}^t(\Psi^0,\mathbf{\Psi}^1)$ in $\mathcal{A}_d$. In (1.7), the function $\chi(f)$ denotes the Eddington factor given by:

$$\chi(f)=\frac{3+4\|f\|^2}{5+2\sqrt{4-3\|f\|^2}}. \tag{1.8}$$

The M1 model is valid in optically thick regimes and for free transport, and interpolates between the two extremes. The case of electron radiotherapy is close to a diffusive regime.

Let us underline, that the system (1.6) is nothing but a system of conservation laws supplemented by a source term. Although the variable ε is the physical energy of the particles, mathematically it can be understood as a time. Indeed, the needed additional condition is

$$\lim_{\varepsilon\to\infty}\Psi^0(\mathbf{x},\varepsilon)=0, \qquad \lim_{\varepsilon\to\infty}\mathbf{\Psi}^1(\mathbf{x},\varepsilon)=0, \tag{1.9}$$

meaning that there are no particles with arbitrary high energy. A practical modification of the condition at infinity is

$$\Psi^0(\mathbf{x},\varepsilon_{\max})=\delta>0, \qquad \mathbf{\Psi}^1(\mathbf{x},\varepsilon_{\max})=0, \tag{1.10}$$

for a relevant choice of $\varepsilon_{\max}$, where δ denotes a small energy value, typically 10^{-10}. If we interpret the energy ε as a mathematical time, this is an initial condition at some $\varepsilon=\varepsilon_{\max}$ and we have to solve the system from $\varepsilon_{\max}$ to 0. We will refer to this solution technique as energy-marching.

As a consequence, the Cauchy problem arising from (1.6) is now given by:

$$\partial_\varepsilon(\rho S\Psi^0)-\nabla\cdot\mathbf{\Psi}^1=0, \qquad \partial_\varepsilon(\rho S\mathbf{\Psi}^1)-\nabla\cdot D_e\Big(\frac{\mathbf{\Psi}^1}{\Psi^0}\Big)\Psi^0=\rho T\mathbf{\Psi}^1, \tag{1.11}$$

where $\varepsilon\in(0,\varepsilon_{\max})$ and with the initial data:

$$\Psi^0(\mathbf{x},\varepsilon_{\max})=\delta, \qquad \mathbf{\Psi^1}(\mathbf{x},\varepsilon_{\max})=0. \tag{1.12}$$

The system (1.6) with constant ρ and S is hyperbolic for all $(\Psi^0,\mathbf{\Psi}^1)$ in $\mathcal{A}_d$ [32]. Moreover, it is proved in [15], that this system has the correct free-streaming limit, and in [23] that it reproduces the diffusion limit of the kinetic equation. Finally, we expect this model to preserve Ψ^0 positive. Several numerical strategies have been developed in the literature [5–7, 11–13, 21–23].

Before introducing the scheme of interest, we note that a first naive discretization of this system consists in separating the energy derivative as:

$$\partial_\varepsilon(\rho S\Psi^0)=\rho S\partial_\varepsilon\Psi^0+\Psi^0\partial_\varepsilon(\rho S),$$

to rewrite the system (2.1) as:

$$\partial_\varepsilon\Psi^0=\frac{1}{\rho S}\Big(\partial_x\Psi^1-\partial_\varepsilon(\rho S)\Big), \tag{1.13a}$$

$$\partial_\varepsilon\mathbf{\Psi}^1=\frac{1}{\rho S}\left(\partial_x\Big(\Psi^0\chi\Big(\frac{\mathbf{\Psi}^1}{\Psi^0}\Big)\Big)+\mathbf{\Psi}^1\big(\rho T-\partial_\varepsilon(\rho S)\big)\right). \tag{1.13b}$$

However, the presence of $\rho(x)$ in front of the flux derivative will be seen to introduce numerical difficulties when ρ has discontinuities. For this reason, we do not adopt this discretization. Instead, we will introduce several transformations, which will eventually lead to a $1/\rho$ inside the x-derivative, i.e., a spatially varying, potentially discontinuous, flux function.

The paper is organized as follows. In the next section, we propose to consider the one dimensional model and show a transformation to deal with the stopping power. Indeed, we remark that the density $\rho(\mathbf{x})$ and the function $S(\varepsilon)$ introduce a distortion of the phase space ($\mathbf{x}$,ε) which makes the numerical approximation difficult. To circumvent this problem, we suggest judicious changes of variables to straighten up the phase space. The resulting numerical scheme will be very accurate and costless, but it does not admit a direct 2D extension. As a consequence, in Section 3, we reformulate this 1D method in order to admit a direct 2D extension. Several numerical experiments (comparisons and convergence tests) will show the relevance of the 1D method and justify the 2D derivation. Section 4 is devoted to the details of the 2D numerical procedure. To illustrate the proposed scheme, several dose calculations with CT data are performed in Section 5.

2 Change of variables in 1D

In the present section, we consider the following system for numerical approximation:

$$\partial_\varepsilon(\rho S\Psi^0)-\partial_x\Psi^1=0,\qquad \partial_\varepsilon(\rho S\Psi^1)-\partial_x\Big(\Psi^0\chi\Big(\frac{\Psi^1}{\Psi^0}\Big)\Big)=\rho T\Psi^1, \tag{2.1}$$

where the solution (Ψ^0,Ψ^1) belongs to the admissible set $\mathcal{A}_1$.

We first consider the homogeneous system associated with (2.1), which we write in the following condensed form:

$$\partial_\varepsilon(\rho SU)-\partial_x F(U)=0, \tag{2.2}$$

where $U={}^t(\Psi^0,\Psi^1)$ denotes the state vector in $\mathcal{A}_1$, while the flux function is defined by:

$$F(U)={}^t\Big(\Psi^1,\Psi^0\chi\Big(\frac{\Psi^1}{\Psi^0}\Big)\Big). \tag{2.3}$$

We first introduce a change of variables to eliminate $\rho(x)$ and $S(\varepsilon)$ from (2.2). An HLL scheme [25] (see also [10, 40]) is then applied.

In a second step, we detail an extension of the introduced HLL scheme to take into account the source term.

2.1 Numerical scheme for the homogeneous system

We consider the homogeneous system (2.2) to focus on the role played by both functions $\rho(x)$ and $S(\varepsilon)$. In order to avoid numerical problems from large variations of the density $\rho(x)$, we propose a convenient change of variables.

First, to get rid of the stopping power in the energy derivative, since $S(\varepsilon)$ does not vanish, we set:

$$\hat{U}(x,\varepsilon)=S(\varepsilon)U(x,\varepsilon), \tag{2.4}$$

to rewrite (2.2) in the following form:

$$S\partial_\varepsilon(\rho\hat{\Psi}^0)-\partial_x\hat{\Psi}^1=0, \qquad S\partial_\varepsilon(\rho\hat{\Psi}^1)-\partial_x\Big(\hat{\Psi}^0\chi\Big(\frac{\hat{\Psi}^1}{\hat{\Psi}^0}\Big)\Big)=0. \tag{2.5}$$

Since the positive density does not depend on energy, we divide the system (2.5) by ρ to write:

$$S\partial_\varepsilon\hat{\Psi}^0-\frac{1}{\rho}\partial_x\hat{\Psi}^1=0, \qquad S\partial_\varepsilon\hat{\Psi}^1-\frac{1}{\rho}\partial_x\Big(\hat{\Psi}^0\chi\Big(\frac{\hat{\Psi}^1}{\hat{\Psi}^0}\Big)\Big)=0. \tag{2.6}$$

Now, we introduce the function $\widetilde{\varepsilon}:\mathbb{R}^+\to\mathbb{R}^+$ by:

$$\widetilde{\varepsilon}(\varepsilon)=\int_0^\varepsilon\frac{1}{S(t)}dt, \tag{2.7}$$

which is well-defined due to the positivity of S. Since S is a positive function, the mapping $\widetilde{\varepsilon}:\varepsilon\mapsto\widetilde{\varepsilon}(\varepsilon)$ is clearly an increasing function. As a consequence, it may be used as a change of variables to define:

$$\bar{U}(x,\widetilde{\varepsilon})=\hat{U}(x,\varepsilon). \tag{2.8}$$

Let us note that the energy derivative now writes as:

$$S(\varepsilon)\partial_\varepsilon\hat{U}(x,\varepsilon)=\partial_{\widetilde{\varepsilon}}\bar{U}(x,\widetilde{\varepsilon}). \tag{2.9}$$

As a consequence, the system (2.6) recasts as follows:

$$\partial_{\widetilde{\varepsilon}}\bar{\Psi}^0(x,\widetilde{\varepsilon})-\frac{1}{\rho(x)}\partial_x\bar{\Psi}^1(x,\widetilde{\varepsilon})=0, \tag{2.10a}$$

$$\partial_{\widetilde{\varepsilon}}\bar{\Psi}^1(x,\widetilde{\varepsilon})-\frac{1}{\rho(x)}\partial_x\Big(\bar{\Psi}^0(x,\widetilde{\varepsilon})\chi\Big(\frac{\bar{\Psi}^1(x,\widetilde{\varepsilon})}{\bar{\Psi}^0(x,\widetilde{\varepsilon})}\Big)\Big)=0. \tag{2.10b}$$

We adopt the same approach to deal with the positive density $\rho(x)$. Hence we set:

$$\widetilde{x}(x)=\int_0^x\rho(t)dt. \tag{2.11}$$

As the density is positive, the function $\widetilde{x}:\mathbb{R}^+\to\mathbb{R}^+$ defines an increasing function, and thus, we consider it as a change of variables to define:

$$\widetilde{U}(\widetilde{x},\widetilde{\varepsilon})=\bar{U}(x,\widetilde{\varepsilon}). \tag{2.12}$$

Since we easily have:

$$\frac{1}{\rho(x)}\partial_x\bar{U}(x,\widetilde{\varepsilon})=\partial_{\widetilde{x}}\widetilde{U}(\widetilde{x},\widetilde{\varepsilon}), \tag{2.13}$$

the system (2.10) gives:

$$\partial_{\widetilde{\varepsilon}}\widetilde{\Psi}^0(\widetilde{x},\widetilde{\varepsilon})-\partial_{\widetilde{x}}\widetilde{\Psi}^1(\widetilde{x},\widetilde{\varepsilon})=0, \tag{2.14a}$$

$$\partial_{\widetilde{\varepsilon}}\widetilde{\Psi}^1(\widetilde{x},\widetilde{\varepsilon})-\partial_{\widetilde{x}}\Big(\widetilde{\Psi}^0(\widetilde{x},\widetilde{\varepsilon})\chi\Big(\frac{\widetilde{\Psi}^1(\widetilde{x},\widetilde{\varepsilon})}{\widetilde{\Psi}^0(\widetilde{x},\widetilde{\varepsilon})}\Big)\Big)=0. \tag{2.14b}$$

To shorten the notations, let us write the system of conservation laws (2.14) as follows:

$$\partial_{\widetilde{\varepsilon}}\widetilde{U}-\partial_{\widetilde{x}}F(\widetilde{U})=0, \tag{2.15}$$

where the flux function F is defined by (2.3). To summarize the sequence of changes of variables (2.4), (2.8) and (2.12), we have the following identity:

$$S(\varepsilon)U(x,\varepsilon)=\widetilde{U}(\widetilde{x},\widetilde{\varepsilon}). \tag{2.16}$$

In order to discretize the system (2.2) on $[0,x_M]$, we propose to approximate (2.15) using a uniform mesh in the tilde variables. For a fixed interval $[0,x_M]$, we apply the space change of variables (2.11) to obtain an interval $[0,\widetilde{x}_M]$ where:

$$\widetilde{x}_M:=\widetilde{x}(x_M)=\int_0^{x_M}\rho(t)dt. \tag{2.17}$$

On this interval, we construct a uniform mesh by setting:

$$\widetilde{x}_{i+\frac{1}{2}}=i\Delta\widetilde{x},\quad\text{with}\quad\Delta\widetilde{x}=\frac{\widetilde{x}_M}{i\max},\quad\text{for }\ 0\le i\le i\max,$$

where $i\max$ is the number of cells. As usual, $\widetilde{x}_{i+1/2}$ denotes the interfaces between cells.

Using the notation $\widetilde{\mathcal{M}}_i=[\widetilde{x}_{i-1/2},\widetilde{x}_{i+1/2}]$ for a cell, we obtain the decomposition

$$\widetilde{\mathcal{M}}=(\widetilde{\mathcal{M}}_i)_{1\le i\le i\max}, \tag{2.18}$$

of $[0,\widetilde{x}_M]$. From the mesh $\widetilde{\mathcal{M}}$, we obtain a non-uniform mesh $\mathcal{M}$ of $[0,x_M]$ by

$$x_{i+\frac{1}{2}}=\widetilde{x}^{-1}\big(\widetilde{x}_{i+\frac{1}{2}}\big), \tag{2.19}$$

where $\widetilde{x}^{-1}$ is the inverse function of $\widetilde{x}$ given by (2.11).

In general, the increment $x_{i+1/2}-x_{i-1/2}$ is not constant. Note that we have $\bigcup_{i=1}^{i\max}\mathcal{M}_i=[0,x_M]$.

Now, we establish a backward HLL scheme for (2.15) on the uniform mesh $\widetilde{\mathcal{M}}$, and a uniform mesh $\widetilde{\varepsilon}^p=p\Delta\widetilde{\varepsilon}$ in energy. As usual, we assume that we are given a piecewise constant approximation $\widetilde{U}^h(\widetilde{\varepsilon}^{p+1},\widetilde{x})$ at energy $\widetilde{\varepsilon}^{p+1}$, defined by:

$$\widetilde{U}^h(\widetilde{\varepsilon}^{p+1},\widetilde{x})=\widetilde{U}_i^{p+1},\qquad\text{if }\ \widetilde{x}\in\widetilde{\mathcal{M}}_i.$$

This approximation is now evolved in energy to define an updated state vector $\widetilde{U}_i^p$ at energy $\widetilde{\varepsilon}^p$. We obtain the following backward HLL scheme:

$$\widetilde{U}_i^p = \widetilde{U}_i^{p+1} - \frac{\Delta\widetilde{\varepsilon}}{\Delta\widetilde{x}}\Big(\widetilde{\mathcal{F}}_{i+\frac{1}{2}}^{p+1} - \widetilde{\mathcal{F}}_{i-\frac{1}{2}}^{p+1}\Big), \tag{2.20}$$

where the numerical flux function is given by:

$$\widetilde{\mathcal{F}}_{i+\frac{1}{2}}^{p+1} = \frac{1}{2}\Big(F(\widetilde{U}_i^{p+1}) + F(\widetilde{U}_{i+1}^{p+1})\Big) - \frac{1}{2}\Big(\widetilde{U}_{i+1}^{p+1} - \widetilde{U}_i^{p+1}\Big).$$

After the work by [25] for instance (see also [10]), the energy increment $\Delta\widetilde{\varepsilon}$ is restricted according to the following CFL like condition:

$$\Delta\widetilde{\varepsilon} \le \frac{\Delta\widetilde{x}}{2}. \tag{2.21}$$

The key idea now is that, due to relation (2.16), we automatically have a scheme for the original untransformed variables:

$$S(\varepsilon_p)U_i^p = S(\varepsilon_{p+1})\Big(U_i^{p+1} - \frac{\Delta\widetilde{\varepsilon}}{\Delta\widetilde{x}}\Big(\mathcal{F}_{i+\frac{1}{2}}^{p+1} - \mathcal{F}_{i-\frac{1}{2}}^{p+1}\Big)\Big), \tag{2.22}$$

where

$$\mathcal{F}_{i+\frac{1}{2}}^{p+1} = \frac{1}{2}\Big(F(U_i^{p+1}) + F(U_{i+1}^{p+1})\Big) - \frac{1}{2}\Big(U_{i+1}^{p+1} - U_i^{p+1}\Big).$$

Let us emphasize that the discretization in the initial variables (x,ε) is not uniform as soon as ρ is not constant. The initial values are discretized on a non-uniform grid. The energy step, however, is performed with a scheme that does not differ from a scheme on a uniform grid.

To conclude with this description of the 1D scheme for the homogeneous system (2.2), the robustness of the method is given in the following statement:

Lemma 2.1. *Let U_i^{p+1} be in $\mathcal{A}_1$, for $1 \le i \le i\max$. We assume that the updated state vector $\widetilde{U}_i^{p+1}$ is given by (2.22). Then, under the CFL condition (2.21), U_i^p is in $\mathcal{A}_1$ for $1 \le i \le i\max$.*

Proof. We assume that U_i^{p+1} belongs to $\mathcal{A}_1$, for all $1 \le i \le i\max$. We thus have the two following relations:

$$(\Psi^0)_i^{p+1} > 0 \quad \text{and} \quad \frac{|(\Psi^1)_i^{p+1}|}{(\Psi^0)_i^{p+1}} < 1.$$

From relation (2.16), we immediately deduce:

$$(\widetilde{\Psi}^0)_i^{p+1} = S(\varepsilon^{p+1})(\Psi^0)_i^{p+1} \quad \text{and} \quad (\widetilde{\Psi}^1)_i^{p+1} = S(\varepsilon^{p+1})(\Psi^1)_i^{p+1}.$$

Since S is a positive function, we have the relations:

$$(\widetilde{\Psi}^0)_i^{p+1}>0 \quad \text{and} \quad \frac{|(\widetilde{\Psi}^1)_i^{p+1}|}{(\widetilde{\Psi}^0)_i^{p+1}}<1,$$

which imply that $\widetilde{U}_i^{p+1}$ belongs to $\mathcal{A}_1$ for all $1\le i\le i\max$. After [10, 25], under the CFL restriction (2.21), the states $\widetilde{U}_i^p$ belong to $\mathcal{A}_1$ for $1\le i\le i\max$, as long as $\widetilde{U}_i^{p+1}\in\mathcal{A}_1$ for $1\le i\le i\max$. Finally, from the relation (2.16) and the positivity property of the function S, we deduce that if $\widetilde{U}_i^p\in\mathcal{A}_1$, and then $U_i^p\in\mathcal{A}_1$. This concludes the proof. □

2.2 Source term discretization

We now reintroduce the source term into the system. In the transformed variables, the initial system (2.1) can be rewritten:

$$\partial_{\widetilde{t}}\widetilde{\Psi}^0(\widetilde{x},\widetilde{\varepsilon})-\partial_{\widetilde{x}}\widetilde{\Psi}^1(\widetilde{x},\widetilde{\varepsilon})=0, \tag{2.23a}$$

$$\partial_{\widetilde{t}}\widetilde{\Psi}^1(\widetilde{x},\widetilde{\varepsilon})-\partial_{\widetilde{x}}\Big(\widetilde{\Psi}^0(\widetilde{x},\widetilde{\varepsilon})\chi\Big(\frac{\widetilde{\Psi}^1(\widetilde{x},\widetilde{\varepsilon})}{\widetilde{\Psi}^0(\widetilde{x},\widetilde{\varepsilon})}\Big)\Big)=\widetilde{T}(\widetilde{\varepsilon})\widetilde{\Psi}^1(\widetilde{x},\widetilde{\varepsilon}), \tag{2.23b}$$

where, according to the change of variables (2.16) and by definition of T given by (1.3), we have:

$$\widetilde{T}(\widetilde{\varepsilon})=T(\varepsilon). \tag{2.24}$$

To discretize the source term, we adopt the source term approximation proposed in [7]. The intermediate state of the Riemann solver is modified in a way that preserves the domain of admissibility. The flux is a convex combination of the HLL flux and a discretization $\widetilde{\Sigma}_i^{p+1}$ of the source term:

$$\widetilde{U}_i^p=\widetilde{U}_i^{p+1}-\frac{\Delta\widetilde{\varepsilon}}{\Delta\widetilde{x}}\alpha\Big(\widetilde{\mathcal{F}}_{i+\frac12}^{p+1}-\widetilde{\mathcal{F}}_{i-\frac12}^{p+1}\Big)+2\,\Delta\widetilde{\varepsilon}\frac{(1-\alpha)}{\Delta\widetilde{x}}\widetilde{\Sigma}_i^{p+1}. \tag{2.25}$$

The parameter $0<\alpha<1$ can be chosen. Here we use a version that guarantees a good behavior for large transport coefficients

$$\alpha=\frac{2}{2+\Delta\widetilde{x}}.$$

Here,

$$\widetilde{\Sigma}_i^{p+1}=\begin{pmatrix}0\\(\widetilde{\Psi}^1)_i^{p+1}\widetilde{T}^{p+1}\end{pmatrix}.$$

Using the relations (2.16) and (2.24), this gives us a scheme for the initial variables (x,ε):

$$S(\varepsilon_p)U_i^p=S(\varepsilon_{p+1})\Big(U_i^{p+1}-\frac{\Delta\widetilde{\varepsilon}}{\Delta\widetilde{x}}\alpha\Big(\mathcal{F}_{i+\frac12}^{p+1}-\mathcal{F}_{i-\frac12}^{p+1}\Big)+2\,\Delta\widetilde{\varepsilon}\frac{(1-\alpha^{p+1})}{\Delta\widetilde{x}}\Sigma_i^{p+1}\Big), \tag{2.26}$$

where

$$\Sigma_i^{p+1}=\begin{pmatrix} 0 \\ (\Psi^1)_i^{p+1}T^{p+1} \end{pmatrix} \quad \text{and} \quad \alpha=\frac{2}{2+\Delta\widetilde{x}}.$$

We call this scheme HLL_{cv}, where the index cv stands for change of variables.

2.3 Validation test

In order to show the validity of the proposed numerical procedure, several numerical experiments are now performed.

The first numerical test is devoted to the approximation of a Riemann problem for (2.23). The initial data consists of two constant states separated by a discontinuity located at $x=0.5$. It is defined as follows:

$$\Psi^0(x,\varepsilon_{\max})=\begin{cases} 0.5, & \text{if } x<0.5, \\ 3, & \text{if } x>0.5, \end{cases} \qquad \Psi^1(x,\varepsilon_{\max})=0. \tag{2.27}$$

In this benchmark, we omit the source term, and thus set $T(\varepsilon)=0$. Furthermore, we set $\varepsilon_{\max}=1$, $S(\varepsilon)=1$, but we prescribe a discontinuous density

$$\rho(x)=\begin{cases} 1, & \text{if } x<0.3, \\ 0.01, & \text{if } 0.3<x<0.5, \\ 1, & \text{if } x>0.5. \end{cases} \tag{2.28}$$

The simulation is performed on the space interval $[0,1]$ discretized with 256 cells, and the approximation is displayed in Fig. 1. The resulting numerical solution Ψ^0 is compared to a reference solution, which was obtained by the same method but with 16384 cells. We observe a fairly good approximation and the numerical diffusion is in agreement with what we expect from the HLL scheme (see [10, 40]). In fact, the main difficulty coming

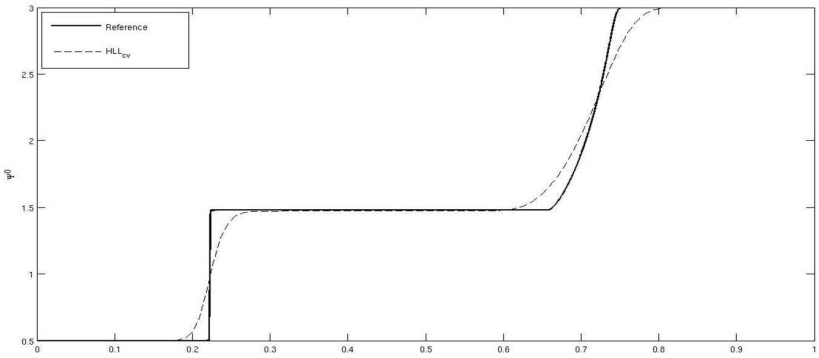

Figure 1: Solution Ψ^0 of the Riemann problem (2.27): reference solution (solid line) and approximated solution by the HLL_{cv} scheme (dashed line) at energy $\varepsilon=0.5$.

with this experiment turns out to be the discontinuities in the density. As expected, the proposed scheme is *independent* of these density discontinuities.

In the next section, this numerical experiment will be compared to another one and several numerical convergence improvements will be detailed.

3 Projection method in 1D

So far, we have derived a specific 1D method for (1.6) based on a suitable change of variables. The main benefit of the detailed changes of variables comes from the independence of the scheme (2.23) on the discontinuous density function $\rho(x)$. This makes the resulting numerical scheme very convenient and the obtained approximate solutions are fairly good.

However, we needed a uniform mesh for the undistorted space $(\widetilde{x},\widetilde{\varepsilon})$. Now, in the goal to extend the method to 2D, let us underline that a global change of variables that eliminates ρ is not possible in general. Indeed, a transformation that satisfies (2.13) with the partial derivative replaced by the divergence operator only exists for constant ρ or a density ρ that does not depend on either x or y. As a consequence, we propose to modify the 1D scheme (2.26) in order to consider a *local* change of variables. Such a modified method must admit an easy 2D derivation. In fact, to obtain the scheme (2.26), we have imposed a uniform mesh $\widetilde{\mathcal{M}}$ while the non-uniform mesh $\mathcal{M}$ was derived from the nodes $\widetilde{x}_{i+1/2}$. In the modification, we enforce the two meshes $\mathcal{M}$ and $\widetilde{\mathcal{M}}$ to be uniform. As a consequence, the nodes $x_{i+1/2}$ are not linked by (2.11), and we have in general,

$$\widetilde{x}_{i+\frac{1}{2}} \neq \widetilde{x}\left(x_{i+\frac{1}{2}}\right).$$

The main discrepancy with the above derived 1D method, is the loss of a direct correspondence between the grid points of the meshes $\mathcal{M}$ and $\widetilde{\mathcal{M}}$. In this section, we introduce a projection technique to transform between the two meshes.

First, we define the two meshes $\mathcal{M}$ and $\widetilde{\mathcal{M}}$ under consideration. We denote by Δx and $\Delta\widetilde{x}$, the respective constant sizes of the cells and set:

$$x_{i+\frac{1}{2}} = i\Delta x, \quad \text{with} \quad \Delta x = \frac{x_M}{i\max},$$
$$\widetilde{x}_{i+\frac{1}{2}} = i\Delta\widetilde{x}, \quad \text{with} \quad \Delta\widetilde{x} = \frac{\widetilde{x}_M}{i\max},$$

where $\widetilde{x}_M$ is still defined by (2.17). Note that both meshes can consist of a different number of cells. However, for simplicity we have taken both meshes to consist of $i\max$ cells. The cells are thus defined by:

$$\mathcal{M}_i = \left[x_{i-\frac{1}{2}}, x_{i+\frac{1}{2}}\right] \quad \text{and} \quad \widetilde{\mathcal{M}}_i = \left[\widetilde{x}_{i-\frac{1}{2}}, \widetilde{x}_{i+\frac{1}{2}}\right].$$

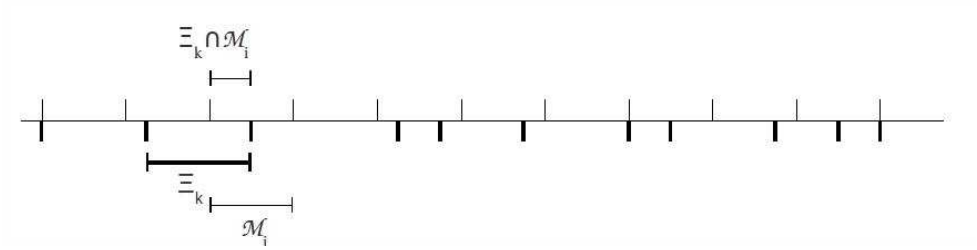

Figure 2: Projection steps in 1D.

For convenience, we denote by x_i and $\widetilde{x}_i$ the center of each cell $\mathcal{M}_i$ and $\widetilde{\mathcal{M}}_i$. Note that we have:

$$\bigcup_{i=1}^{i\max} \mathcal{M}_i = [0, x_M] \quad \text{and} \quad \bigcup_{i=1}^{i\max} \widetilde{\mathcal{M}}_i = [0, \widetilde{x}_M].$$

At each energy ε^{p+1}, the state vector U_i^{p+1} is known on the mesh $\mathcal{M}$. To evolve $(U_i^{p+1})_{1\le i\le i\max}$ to $(U_i^p)_{1\le i\le i\max}$, we will use the scheme (2.25) on the mesh $\widetilde{\mathcal{M}}$. As a consequence, we have to determine $\widetilde{U}_i^{p+1}$ on the mesh $\widetilde{\mathcal{M}}$. Our purpose is now to establish a relevant projection step from $\mathcal{M}$ to $\widetilde{\mathcal{M}}$ to evaluate $\widetilde{U}_i^{p+1}$. In order to preserve the conservation to be satisfied by the scheme, we impose the projection to be conservative. We introduce a third non-uniform mesh Ξ, to discretize $[0, x_M]$, made of the nodes $\xi_{i+1/2}$ defined by:

$$\xi_{i+\frac{1}{2}} = \widetilde{x}^{-1}(\widetilde{x}_{i+\frac{1}{2}}),$$

where $\widetilde{x}^{-1}$ is the inverse of $\widetilde{x}$ given by (2.11). We denote by ξ_i the center of the cell $\Xi_i = [\xi_{i-1/2}, \xi_{i+1/2}]$. Let us note that the mesh Ξ exactly coincides with the non uniform mesh $\mathcal{M}$, defined by (2.19), which we obtained in 1D from the change of variables. Clearly, as soon as the state vector is known at each cell Ξ for $1 \le i \le i\max$, the scheme (2.25)-(2.26) can be applied involving the meshes Ξ and $\widetilde{\mathcal{M}}$.

We define the projection $\widetilde{\Pi}$, which gives the piecewise constant function $\widetilde{U}$ on the mesh $\widetilde{\mathcal{M}}$ from the solution U on the mesh $\mathcal{M}$, by the relation:

$$(\widetilde{\Pi} U)_i^p = S(\varepsilon^p) \sum_{k=1}^{i\max} \widetilde{a}_{i,k} U_k^p \quad \text{and} \quad \widetilde{a}_{i,k} = \frac{\text{meas}(\Xi_k \cap \mathcal{M}_i)}{\text{meas}(\mathcal{M}_i)}, \tag{3.1}$$

where the coefficient $\widetilde{a}_{i,k}$ is the ratio of the lengths of the cells $\Xi_k \cap \mathcal{M}_i$ and $\mathcal{M}_i$ (see Fig. 2). In fact, we note that $\sum_{k=1}^{i\max} \widetilde{a}_{i,k} U_k^p$ is nothing but the projected value of the state vector U_i^p on the cell Ξ_i. Hence, a direct application of the change of variables (2.16) yields to the projection definition (3.1). For fixed $1 \le i \le i\max$, let us underline that, by definition of $\widetilde{a}_{i,k} \ge 0$, we have:

$$\sum_{k=1}^{i\max} \widetilde{a}_{i,k} = 1.$$

As a consequence, we preserve the required conservation property as follows:

$$\sum_{i=1}^{i\max} U_i^p = \sum_{i=1}^{i\max} \Big(\sum_{k=1}^{i\max} \widetilde{a}_{i,k} U_k^p \Big).$$

Reversely, we define the projection which gives U on the mesh $\mathcal{M}$ from the solution $\widetilde{U}$ on the mesh $\widetilde{\mathcal{M}}$. This second projection reads as follows:

$$(\Pi \widetilde{U})_i^p = \frac{1}{S(\varepsilon^p)} \sum_{k=1}^{i\max} a_{i,k} \widetilde{U}_k^p \quad \text{and} \quad a_{i,k} = \frac{\text{meas}(\mathcal{M}_k \cap \Xi_i)}{\text{meas}(\Xi_i)}. \tag{3.2}$$

Once again, the projection Π is conservative since we have:

$$\sum_{i=1}^{i\max} \widetilde{U}_i^p = \sum_{i=1}^{i\max} \Big(\sum_{k=1}^{i\max} \widetilde{a}_{i,k} \widetilde{U}_k^p \Big).$$

To conclude the introduction of the projections, we remark that Π and $\widetilde{\Pi}$ do not commute: $\Pi(\widetilde{\Pi} U) \neq \widetilde{\Pi}(\Pi U)$.

Involving the above projections, we exhibit a numerical procedure from $(U_i^{p+1})_{0\leq i\leq i\max}$ to evaluate $(U_i^p)_{1\leq i\leq i\max}$. This numerical scheme summarizes as follows:

1. From the state vectors $(U_i^{p+1})_{1\leq i\leq i\max}$ on the mesh $\mathcal{M}$ and at the energy ε^{p+1}, we evaluate $(\widetilde{U}_i^{p+1})_{1\leq i\leq i\max}$ on the mesh $\widetilde{\mathcal{M}}$, by the projection $\widetilde{\Pi}$:
$$\widetilde{U}_i^{p+1} = (\widetilde{\Pi} U)_i^{p+1}, \quad \text{for } \ 1\leq i\leq i\max.$$
2. We apply the scheme (2.25) to get the updated state vectors $(\widetilde{U}_i^p)_{1\leq i\leq i\max}$ on the mesh $\widetilde{\mathcal{M}}$.
3. We re-project the solution $(\widetilde{U}_i^p)_{1\leq i\leq i\max}$ from the mesh $\widetilde{\mathcal{M}}$ on the initial mesh $\mathcal{M}$ thanks to the operator Π:
$$U_i^p = (\Pi \widetilde{U})_i^p, \quad \text{for } \ 1\leq i\leq i\max.$$

For the sake of clarity in the notations, this numerical procedure will be called $(2.25)_{\widetilde{\Pi}}$-$(2.26)_{\Pi}$ in the sequel.

The robustness of the method is established in the following result:

Lemma 3.1. *Let U_i^{p+1} be in $\mathcal{A}_1$ for $1\leq i\leq i\max$. Assume that the updated state vectors U_i^p to be given by the numerical procedure $(2.25)_{\widetilde{\Pi}}$-$(2.26)_{\Pi}$. Under the CFL like restriction (2.21), for all $1\leq i\leq i\max$, U_i^p belongs to $\mathcal{A}_1$.*

Proof. Since the projection step $\widetilde{\Pi}$ is made of a convex combination of vectors U_i^{p+1}, as soon as $U_i^{p+1}\in\mathcal{A}_1$ for all $1\leq i\leq i\max$, the projected vectors $\widetilde{U}_i^{p+1}$ is still in $\mathcal{A}_1$. Indeed, $\mathcal{A}_1$ is a convex set. After [25], under the CFL condition (2.21), the HLL scheme (2.25) preserves the admissible states. As a consequence, we immediately deduce that $\widetilde{U}_i^p$ is in $\mathcal{A}_1$, for all $1\leq i\leq i\max$. Finally, the re-projection of the solution in $\mathcal{M}$, which is made of convex combinations of elements of $\widetilde{U}_i^p$, preserves the admissibility of U_i^p. Hence, U_i^p is in $\mathcal{A}_1$, for all $1\leq i\leq i\max$, and the proof is completed. □

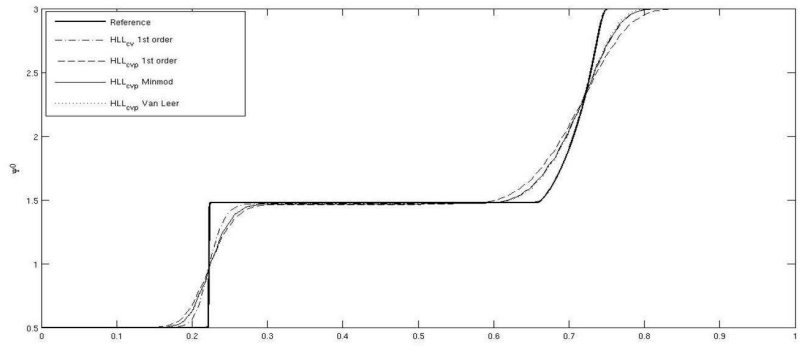

Figure 3: Solution of a Riemann problem performed with a first order HLL_{cv} scheme, a first order HLL_{cvp} scheme, and two second order HLL_{cvp} schemes with minmod and Van Leer limiters at energy $\varepsilon=0.5$.

To validate the scheme $(2.25)_{\widetilde{\Pi}}$-$(2.26)_{\Pi}$, we solve the Riemann problem (2.27), where the density ρ and the function S are defined by (2.28). This scheme, involving projection steps, will be called HLL_{cvp}. The index stands for change of variables with projection.

The obtained numerical results, with a mesh made of 256 cells, are displayed Fig. 3, where we compare the results obtained with first and second order schemes. The second order accuracy is obtained when considering a standard MUSCL method (see [3,4,31,43]). Here, we have adopted the well-known minmod and Van Leer limitation procedures.

Table 1 shows the L^1, L^2 and L^∞ errors evaluated on several mesh refinements. First of all, we notice that the first order method with projections roughly gives the same accuracy as the method without projection by taking twice more cells. As a consequence, the convergence rates of these two methods are similar. Moreover, it is to note that the accuracy with the MUSCL correction of the HLL_{cvp} method is slightly better than the first order HLL_{cv}. Here, the use of MUSCL techniques for the HLL_{cvp} scheme only marginally improves the order of convergence due to the projection steps. This example validates the HLL_{cvp} approach which will be extended to two dimensions in the next section.

4 Projection method in 2D

The present section is devoted to extend the above 1D scheme to approximate the solutions of the 2D model (1.6). To shorten the notations, we write our model as follows:

$$\partial_\varepsilon(\rho SU)-\partial_x F(U)-\partial_y G(U)=\Sigma(U), \tag{4.1}$$

where $U={}^t(\Psi^0,\Psi^1_x,\Psi^1_y)$ is the state vector in $\mathcal{A}_2$ and the flux functions F and G are defined as follows:

$$F(U)=\begin{pmatrix}\Psi^1_x\\ \Psi^0\frac{1-\chi}{2}+\frac{3\chi-1}{2\|\Psi^1\|^2}(\Psi^1_x)^2\\ \Psi^0\frac{3\chi-1}{2\|\Psi^1\|^2}\Psi^1_y\Psi^1_x\end{pmatrix},\qquad G(U)=\begin{pmatrix}\Psi^1_x\\ \Psi^0\frac{3\chi-1}{2\|\Psi^1\|^2}\Psi^1_x\Psi^1_y\\ \Psi^0\frac{1-\chi}{2}+\frac{3\chi-1}{2\|\Psi^1\|^2}(\Psi^1_y)^2\end{pmatrix}. \tag{4.2}$$

Table 1: Comparisons of L^1, L^2, L^∞ errors.

Method	number of cells	L^∞ error	L^2 error	L^1 error	order
	32	0.5596	0.2065	0.1390	
	64	0.4812	0.1585	9.6021×10^{-2}	0.5339
1st order	128	0.4214	0.1186	6.1040×10^{-2}	0.6536
HLL_{cv}	256	0.3907	8.5568×10^{-2}	3.8265×10^{-2}	0.6737
	512	0.3971	6.2348×10^{-2}	2.3751×10^{-2}	0.6881
	1024	0.3911	4.2702×10^{-2}	1.3884×10^{-2}	0.7746
	2048	0.3455	2.7246×10^{-2}	7.4848×10^{-3}	0.8914
	32	0.6553	0.2438	0.1908	
	64	0.5620	0.2002	0.1468	0.3780
1st order	128	0.5028	0.1530	9.5539×10^{-2}	0.6200
HLL_{cvp}	256	0.4679	0.1148	5.9349×10^{-2}	0.6869
	512	0.4523	8.5882×10^{-2}	3.7806×10^{-2}	0.6506
	1024	0.4476	6.1713×10^{-2}	2.3219×10^{-2}	0.7033
	2048	0.3960	4.2469×10^{-2}	1.3518×10^{-2}	0.7804
	32	0.6162	0.2312	0.1740	
	64	0.5271	0.1744	0.1208	0.5263
2nd order	128	0.5167	0.1281	7.3075×10^{-2}	0.7255
Minmod	256	0.4664	9.4580×10^{-2}	4.3889×10^{-2}	0.7355
HLL_{cvp}	512	0.4461	6.9677×10^{-2}	2.7110×10^{-2}	0.6950
	1024	0.4419	4.9287×10^{-2}	1.5938×10^{-2}	0.7663
	2048	0.3999	3.3321×10^{-2}	8.7471×10^{-3}	0.8656
	32	0.6208	0.2278	0.1683	
	64	0.5315	0.1706	0.1170	0.5241
2nd order	128	0.5153	0.1239	6.8487×10^{-2}	0.7730
Van Leer	256	0.4638	9.1065×10^{-2}	4.0879×10^{-2}	0.7445
HLL_{cvp}	512	0.4444	6.7074×10^{-2}	2.5365×10^{-2}	0.6885
	1024	0.4411	4.7387×10^{-2}	1.4715×10^{-2}	0.7856
	2048	0.3772	3.1995×10^{-2}	7.9505×10^{-3}	0.8882

Here, the source term Σ reads:

$$\Sigma(U) = {}^t(0, \rho T \Psi^1_x, \rho T \Psi^1_y). \tag{4.3}$$

The proposed 2D extension consists of a direction splitting to deal first with the x-direction where the system reads:

$$\partial_\varepsilon \rho S U - \partial_x F(U) = 0, \tag{4.4}$$

and next to consider the y-direction system given by:

$$\partial_\varepsilon \rho S U - \partial_y G(U) = 0. \tag{4.5}$$

Concerning the source term, a specific treatment will be adopted by a 2D extension of the method detailed in [7]. The approximated scheme involved per direction is given by

$(2.25)_{\widetilde{\Pi}}$-$(2.26)_{\Pi}$ where a suitable attention is paid on the density which now depends on x and y.

First of all, let us define all the needed meshes. Here, we are looking for solutions on the domain $\Omega=[0,x_M]\times[0,y_M]\subset\mathbb{R}^2$. We adopt a uniform Cartesian mesh by setting $(x_{i+1/2},y_{j+1/2})$, for all $0\le i\le i\max$ and $0\le j\le j\max$, where

$$x_{i+\frac{1}{2}}=i\Delta x,\quad \text{with}\quad \Delta x=\frac{x_M}{i\max},$$
$$y_{j+\frac{1}{2}}=j\Delta y,\quad \text{with}\quad \Delta y=\frac{y_M}{j\max}.$$

For a fixed j, we deduce the pseudo 1D mesh given by $\mathcal{M}=(\mathcal{M}_i)_{1\le i\le i\max}$ made of the cells:

$$\mathcal{M}_i=[x_{i-\frac{1}{2}},x_{i+\frac{1}{2}}],$$

so that $\bigcup_{i=1}^{i\max}\mathcal{M}_i=[0,x_M]$. Similarly, we set $\mathcal{N}=(\mathcal{N}_j)_{1\le j\le j\max}$, the 1D mesh made of the cells:

$$\mathcal{N}_j=\left[y_{j-\frac{1}{2}},y_{j+\frac{1}{2}}\right],$$

so that $\bigcup_{j=1}^{j\max}\mathcal{N}_j=[0,y_M]$.

We denote by x_i and y_j the centers of $\mathcal{M}_i$ and $\mathcal{N}_j$ respectively. Let us remark that we have the following writing of Ω:

$$\bigcup_{j=1}^{j\max}\Big(\bigcup_{i=1}^{i\max}\mathcal{M}_i\times\left[y_{j-\frac{1}{2}},y_{j+\frac{1}{2}}\right]\Big)=[0,x_M]\times[0,y_M],$$

or similarly,

$$\bigcup_{i=1}^{i\max}\Big(\bigcup_{j=1}^{j\max}\mathcal{N}_j\times\left[x_{i-\frac{1}{2}},x_{i+\frac{1}{2}}\right]\Big)=[0,x_M]\times[0,y_M].$$

Now, for a fixed j we consider the 1D mesh $\mathcal{M}\times\{y_j\}$ to apply the following change of variables:

$$\widetilde{x}(x,y_j)=\int_0^x\rho(t,y_j)dt, \tag{4.6}$$

which is directly deduced from (2.11). We set

$$\widetilde{x}_M^j=\widetilde{x}(x_M,y_j),$$

to define a uniform mesh denoted $\widetilde{\mathcal{M}}^j$ of $[0,\widetilde{x}_M^j]$. In fact, this mesh $\widetilde{\mathcal{M}}^j$ coincides with (2.18) but for the 2D extension with a fixed y_j. The cells of $\widetilde{\mathcal{M}}^j$ are defined by:

$$\widetilde{\mathcal{M}}_i^j=[\widetilde{x}_{i-\frac{1}{2}}^j,\widetilde{x}_{i+\frac{1}{2}}^j],$$

where we have set

$$\widetilde{x}^j_{i+\frac{1}{2}} = i\Delta\widetilde{x}_j, \quad \text{with} \quad \Delta\widetilde{x}_j = \frac{\widetilde{x}_j}{i\max}.$$

The center of $\widetilde{\mathcal{M}}^j_i$ will be denoted $\widetilde{x}^j_i$.

Next, a similar mesh definition is adopted in the y-direction. For fixed i, the following change of variables:

$$\widetilde{y}(x_i,y) = \int_0^y \rho(x_i,s)ds \tag{4.7}$$

is applied to the 1D mesh $\{x_i\}\times\mathcal{N}$. Such a change of variables is nothing but the y-extension of (2.11). We set:

$$\widetilde{y}^i_M = \widetilde{y}(x_i,y_M),$$

to derive the uniform mesh $\widetilde{\mathcal{N}}^i$ made of the cells:

$$\widetilde{\mathcal{N}}^i_j = \left[\widetilde{y}^i_{j-\frac{1}{2}},\widetilde{y}^i_{j+\frac{1}{2}}\right],$$

where we have set:

$$\widetilde{y}^i_{j+\frac{1}{2}} = j\Delta\widetilde{y}_i, \quad \text{with} \quad \Delta\widetilde{y}_i = \frac{\widetilde{y}_i}{j\max}.$$

We denote by $\widetilde{y}^i_j$ the center of the cells $\widetilde{\mathcal{N}}^i_j$.

The proposed numerical procedure consists in applying the 1D scheme $(2.25)_{\widetilde{\Pi}}$-$(2.26)_{\Pi}$ in the x-direction for all fixed j when the mesh $\mathcal{M}\times\{y_j\}$ is considered. Next the scheme $(2.25)_{\widetilde{\Pi}}$-$(2.26)_{\Pi}$ is, once again, applied but for the y-direction with a fixed i when considering the 1D mesh $\{x_i\}\times\mathcal{N}$. Therefore the projections, $\widetilde{\Pi}$ and Π defined by (3.1) and (3.2) respectively, must be derived for all the meshes $\mathcal{M}\times\{y_j\}$ and $\{x_i\}\times\mathcal{N}$.

First, we define the projections $\widetilde{\Pi}^j_x$ and Π^j_x (see Fig. 4). According to (3.1) and (3.2), we set:

$$(\widetilde{\Pi}^j_x U)^p_i = S(\varepsilon^p)\sum_{k=1}^{i\max}\widetilde{a}^j_{i,k}U^p_{k,j}, \tag{4.8a}$$

$$(\Pi^j_x \widetilde{U})^p_i = \frac{1}{S(\varepsilon^p)}\sum_{k=1}^{i\max}a^j_{i,k}\widetilde{U}^p_{k,j}, \tag{4.8b}$$

with

$$\widetilde{a}^j_{i,k} = \frac{\text{meas}(\Xi^j_{x,k}\cap\mathcal{M}_i)}{\text{meas}(\mathcal{M}_i)}, \qquad a^j_{i,k} = \frac{\text{meas}(\mathcal{M}_k\cap\Xi^j_{x,i})}{\text{meas}(\Xi^j_{x,i})},$$

where we have introduced:

$$\Xi^j_{x,i} = \left[\xi^j_{x,i-\frac{1}{2}},\xi^j_{x,i+\frac{1}{2}}\right], \qquad \xi^j_{x,i+\frac{1}{2}} = \widetilde{x}^{-1}_j(x_{i+\frac{1}{2}}),$$

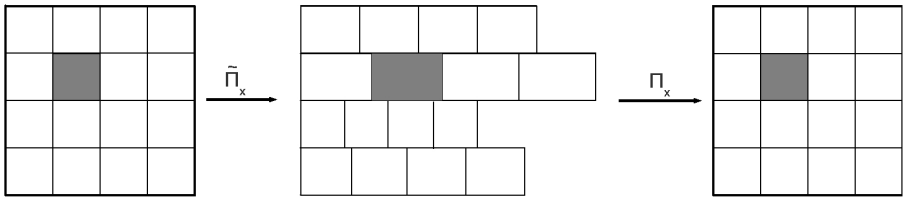

Figure 4: Projection steps in direction x.

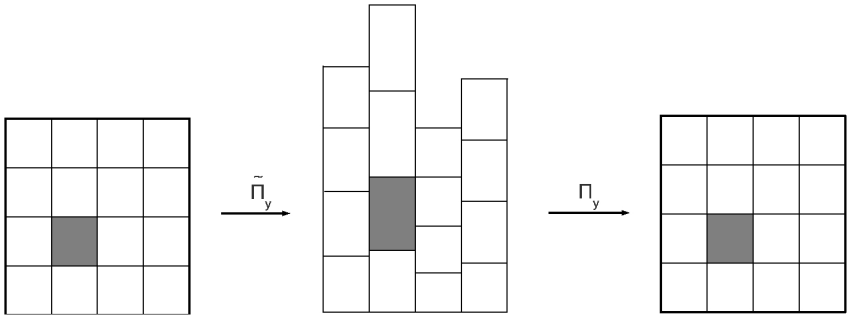

Figure 5: Projection steps in direction y.

where $\widetilde{x}^{-1}$ denotes the inverse of the mapping $x\mapsto\widetilde{x}(x,y_j)$ defined by (4.6). Next, considering the y-direction, we introduce the projections $\widetilde{\Pi}_y^i:\mathcal{N}\times\{x_i\}\to\widetilde{\mathcal{N}}^i$ and $\Pi_y^i:\ \widetilde{\mathcal{N}}^i\to\mathcal{N}\times\{x_i\}$ (see Fig. 5), defined by:

$$(\widetilde{\Pi}_y^i U)_j^p = S(\varepsilon^p)\sum_{k=0}^{j\max}\widetilde{b}_{k,j}^i U_{i,k}^p, \tag{4.9a}$$

$$(\Pi_y^i \widetilde{U})_j^p = \frac{1}{S(\varepsilon^p)}\sum_{k=0}^{j\max} b_{k,j}^i \widetilde{U}_{i,k}^p, \tag{4.9b}$$

with

$$\widetilde{b}_{k,j}^i = \frac{\mathrm{meas}(\Xi_{y,k}^i\cap\mathcal{N}_j)}{\mathrm{meas}(\mathcal{N}_j)}, \qquad b_{k,j}^i = \frac{\mathrm{meas}(\mathcal{N}_k\cap\Xi_{y,j}^i)}{\mathrm{meas}(\Xi_{y,j}^i)},$$

where we have set:

$$\Xi_{y,j}^i = [\xi_{y,j-\frac{1}{2}}^i,\xi_{y,j+\frac{1}{2}}^i], \qquad \xi_{y,j+\frac{1}{2}}^i = \widetilde{y}_i^{-1}(y_{j+\frac{1}{2}}),$$

where $\widetilde{y}^{-1}$ denotes the inverse of the mapping $y\mapsto\widetilde{y}(x_i,y)$ defined by (4.7).

Equipped with these projections, we are able to describe the numerical procedure to evolve the numerical approximate solution $U_{i,j}^{p+1}$ to get $U_{i,j}^p$. Involving a space splitting technique, a two step method is adopted.

• The first step is devoted to evolve in the x-direction. For a fixed j we define the state vectors $(\widetilde{U}_{i,j}^{p+1/2})_{1\leq i\leq i\max}$ by using the projection mapping (4.8a). This state is next evolved in energy when considering an HLL scheme with source term in the form (2.25). The scheme reads

$$\widetilde{U}_{i,j}^{p+\frac{1}{2}}=\widetilde{U}_{i,j}^{p+1}-\frac{\Delta\widetilde{\varepsilon}}{\Delta\widetilde{x}}\alpha_x\Big(\widetilde{\mathcal{F}}_{i+\frac{1}{2},j}^{p+1}-\widetilde{\mathcal{F}}_{i-\frac{1}{2},j}^{p+1}\Big)+2\Delta\widetilde{\varepsilon}\frac{(1-\alpha_x)}{2\Delta\widetilde{x}}\widetilde{\Sigma}_{i,j}^{p+1}, \tag{4.10}$$

where:

$$\widetilde{\mathcal{F}}_{i+\frac{1}{2},j}^{p+1}=\frac{1}{2}\Big(F(\widetilde{U}_{i,j}^{p+1})+F(\widetilde{U}_{i+1,j}^{p+1})\Big)-\frac{1}{2}\Big(\widetilde{U}_{i+1,j}^{p+1}-\widetilde{U}_{i,j}^{p+1}\Big)\quad\text{and}\quad\alpha_x=\frac{2}{2+\Delta\widetilde{x}}, \tag{4.11}$$

and

$$\widetilde{\Sigma}_{i,j}^{p+1}=\begin{pmatrix}0\\ \widetilde{T}^{p+1}(\widetilde{\Psi}_x^1)_{i,j}^{p+1}\\ \widetilde{T}^{p+1}(\widetilde{\Psi}_y^1)_{i,j}^{p+1}\end{pmatrix}. \tag{4.12}$$

This first step is concluded by the projection of the state vectors $(\widetilde{U}_{i,j}^{p+1/2})_{1\leq i\leq i\max}$ by the mapping (4.8b) to get $(U_{i,j}^{p+1/2})_{1\leq i\leq i\max}$ for all $1\leq j\leq j\max$.

• During the second step, the evolution of $U_{i,j}^{p+1/2}$ is performed in the y-direction. For all fixed i from 1 to $i\max$, the projection (4.9a) is used to define the state vectors $(\widetilde{U}_{i,j}^{p+1/2})_{1\leq j\leq j\max}$. These vectors are now evolved in energy by the following HLL scheme:

$$\widetilde{U}_{i,j}^{p}=\widetilde{U}_{i,j}^{p+\frac{1}{2}}-\frac{\Delta\widetilde{\varepsilon}}{\Delta\widetilde{y}}\alpha_y\Big(\widetilde{\mathcal{G}}_{i,j+\frac{1}{2}}^{p+\frac{1}{2}}-\widetilde{\mathcal{G}}_{i,j-\frac{1}{2}}^{p+\frac{1}{2}}\Big)+2\Delta\widetilde{\varepsilon}\frac{(1-\alpha_y)}{2\Delta\widetilde{y}}\widetilde{\Sigma}_{i,j}^{p+\frac{1}{2}}, \tag{4.13}$$

where

$$\widetilde{\mathcal{G}}_{i,j+\frac{1}{2}}^{p+\frac{1}{2}}=\frac{1}{2}\Big(G(\widetilde{U}_{i,j}^{p+\frac{1}{2}})+G(\widetilde{U}_{i,j+1}^{p+\frac{1}{2}})\Big)-\frac{1}{2}\Big(\widetilde{U}_{i,j+1}^{p+\frac{1}{2}}-\widetilde{U}_{i,j}^{p+\frac{1}{2}}\Big)\quad\text{and}\quad\alpha_y=\frac{2}{2+\Delta\widetilde{y}}, \tag{4.14}$$

and

$$\widetilde{\Sigma}_{i,j}^{p+\frac{1}{2}}=\begin{pmatrix}0\\ \widetilde{T}^{p+\frac{1}{2}}(\widetilde{\Psi}_x^1)_{i,j}^{p+\frac{1}{2}}\\ \widetilde{T}^{p+\frac{1}{2}}(\widetilde{\Psi}_y^1)_{i,j}^{p+\frac{1}{2}}\end{pmatrix}. \tag{4.15}$$

Finally, by the projection (4.9b), we deduce the expected updated state vectors $U_{i,j}^{p}$.

4.1 Validation test

In order to validate the proposed 2D numerical technique, we consider an experiment which has a spherical symmetry. A source is applied in a 1cm-radius sphere in a material made of a sequence of variable densities as follows:

$$\rho(r)=\begin{cases}1, & \text{if } 1<r\leq 2,\\ 0.25, & \text{if } 2<r\leq 3,\\ 0.1, & \text{if } 3<r\leq 4,\\ 2, & \text{otherwise.}\end{cases}$$

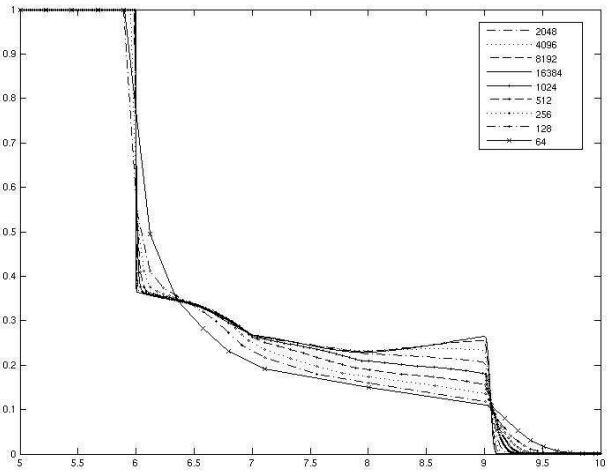

Figure 6: Spherical case: Ψ^0 predicted by the 1D code with a mesh refinement from 128 to 16384 cells.

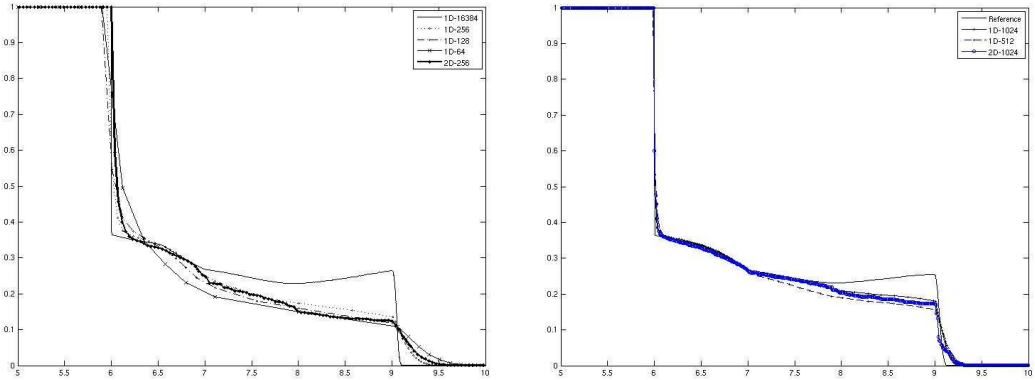

Figure 7: Spherical case: Ψ^0 predicted by the 2D code with 256×256 cells (left) and 1024×1024 cells (right) and cut line along the x axis (below).

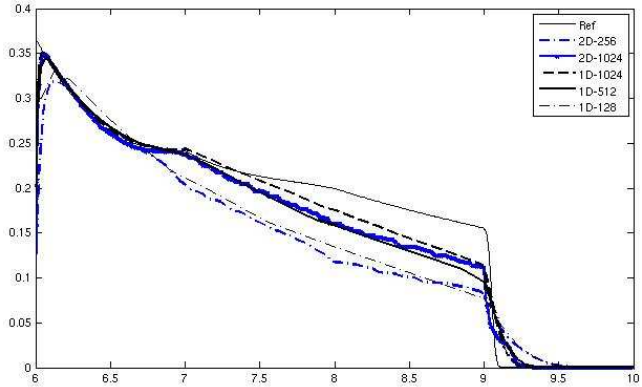

Figure 8: Spherical case: Ψ^1 predicted by the 2D code with 256×256 cells and 1024×1024 cells and cut line along the x axis (below).

The goal of this test-case is to validate the projection procedures. We simplify the model by considering $T=0$, $S=1$, $\varepsilon_{\max}=2.5$ and $\mathbf{\Psi}^2=\Psi^0\mathbf{I}_d/3$. One of the interests of such an experiment is that the system reduces to a one dimension problem using the polar coordinates. Indeed we have:

$$\partial_\varepsilon(r\Psi^0)+\partial_r(r\Psi^1)=0, \qquad \partial_\varepsilon(r\Psi^1)+\partial_r\Big(\frac{r\Psi^0}{3}\Big)=\frac{r\Psi^0}{3r}.$$

Using the variables $(r\Psi^0,r\Psi^1)$ this system turns out to be a 1D model with source term. Therefore, it can be discretized using the 1D procedure described above to compute a reference solution to be compared with the full 2D model. Let us emphasize that such a benchmark is very stiff and a lot of points are required in order to obtain a converged 1D approximation as shown in Fig. 6 for $\varepsilon=0$.

Since the derived 2D numerical procedure is based on a Cartesian grid, the approximation of a spherical solution is challenging due to the multiple projections. Figs. 7 and 8 show the results at energy $\varepsilon=0$ computed on respectively a 256×256 and 1024×1024 grids.

As expected, the results of the 2D scheme are in fairly good agreement with the reference solution.

5 Application to dose calculation

We took a two-dimensional slice of three-dimensional CT data from the Visible Human data set. We apply our model to a case from the literature, a case of an irradiation of the head with electrons [30]. The setting is shown in Fig. 9. It shows a horizontal cut through a human head. In each of the voxels, the material is described by its Hounsfield grey value $\mathcal{G}(x,y)$. The grey values can be translated into physical parameters as follows,

$$\rho(x,y)=\Big(\frac{\mathcal{G}(x,y)}{1000}+1\Big)\rho_W,$$

where ρ_W is the density of water. Dark regions have low density, bright regions higher density. Black is air with a density of approximately 10^{-3}kg/m^3, gray is water with roughly 1kg/m^3, and light gray is bone with about 2kg/m^3. On the right side a bolus made of plastic is attached. In practice, this is used to shape the electron beam.

The head is irradiated from the right with a 12MeV electron beam of width 14cm. To model the incoming beams, we have taken a very narrow Gaussian in energy, and a δ pulse in angle. Other energy spectra are possible. From these, the angular moments $\psi^{(0)}$ and $\psi^{(1)}$ have to be computed, which are used in the code.

As a comparison to our method, we use the state-of-the-art Monte Carlo code PENELOPE [36]. This code has been extensively validated against experimental results. The code solves a far more complicated transport equation with many more physical effects than our model. Both physics models are completely independent. We use PENELOPE as a black box and consider its results as benchmark experimental results.

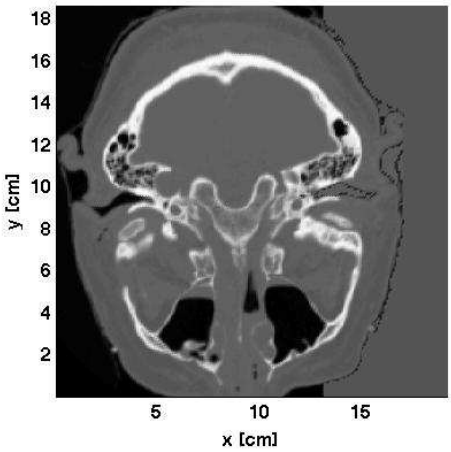

Figure 9: Cut through CT scan of head, with bolus attached to the right.

PENELOPE was set up in a pseudo-2D setting with a large beam size perpendicular to the plane in which the beam propagated. We have used penEasy2009 in a voxelized geometry with standard simulation parameters. The energy cutoff for the initial source energy was set to 15MeV. Electrons and positrons are assumed to be absorbed when their energy becomes less than 150keV. For photons, this value was set to 15keV. The critical angle θ_c and critical energy W_c that separate hard events and soft events was set in the following way: for inelastic collisions, we set $W_c = 150$keV, for bremsstrahlung emission $W_c = 15$keV. The average angular deflection between consecutive hard elastic events $C_1 = 0.1$ and the maximum average fractional energy loss between consecutive hard elastic events $C_2 = 0.1$ uniquely determine θ_c. The maximum allowed step length for electrons and positrons is set to infinity: $DSMAX = 10^{35}$cm. No variance reduction method was used. Let us note that the physical models entering our code are independent from the physical models underlying *penEasy*.

Fig. 10 shows the isodose curves obtained with both methods. The 10%, 25%, 50%, 70% and 80% lines are shown. The statistical noise of the Monte Carlo (MC) solution can be seen in the 80% curve. We can also see that the M1 result is slightly more diffusive than the MC solution, i.e., the beam is a bit wider and the contours for the lower values are further apart. The orange curve even encompasses the void region toward the bottom. But note that this is just the 10% dose curve, so it is not very relevant to the overall irradiation. The major difference, however, is that the M1 model does not produce the same buildup region as the MC solution. this can be seen by the difference in the 80% curves near the boundary. In a previous paper [17], this shortcoming has been attributed to the M1 model, and not the numerical scheme.

Fig. 11 shows a difference plot of the two solutions. In radiotherapy dose calculation, methods are compared by their relative error in the dose and in terms of distance-to-agreement. Overall, about 63% of the voxels are within 4% or 4mm distance-to-

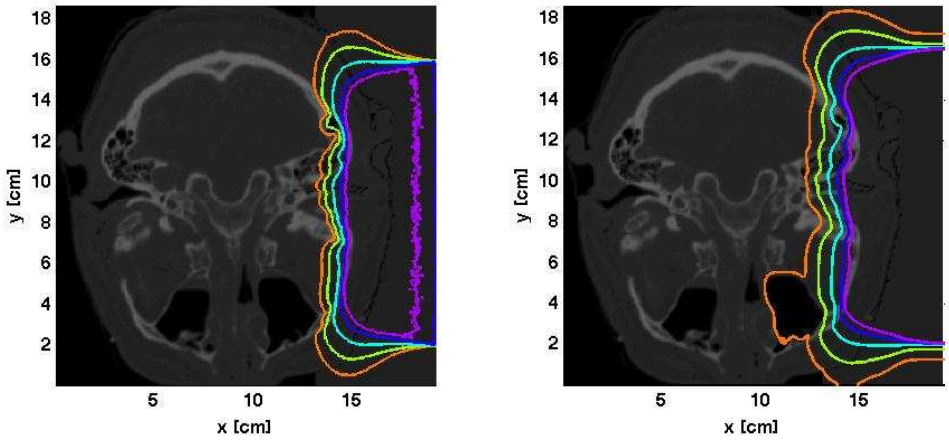

Figure 10: Isodose curves for electron beam on vertebral column. Normalized by $D_{\max}$, they are shown as 10% orange, 25% yellow, 50% light blue, 70% dark blue, 80% violet.

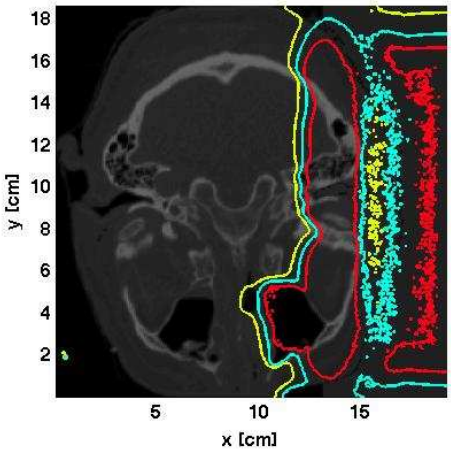

Figure 11: Contour plot of the dose differences between the M1 model and PENELOPE, scaled by the maximum dose (2% difference shown in yellow, 5% difference cyan, 10% difference red).

agreement. This is of course not sufficient to be relevant in practice yet. The reason are mainly due to an oversimplified physical model and shortcomings in the M1 model.

However, it can serve as a prove of concept. The HLL_{cvp} method gives a good approximation of the dose. It has no statistical noise, which is an advantage of deterministic methods. In our numerical experiments, the code using the HLL_{cvp} method needed about 50 minutes on 12 cores, while PENELOPE runs for roughly one day. Of course, this comparison is not fair, since PENELOPE runs in a pseudo-2D setting. But if we extrapolate the computational results to 3D, we can expect an advantage for the deterministic method.

Acknowledgments

The authors would like to thank Bruno Dubroca for helpful comments and fruitful discussions, and Edgar Olbrant for performing the PENELOPE computations. The CT data has been provided by the National Library of Medicine as part of the Visible Human Project. The second author was partially supported by the Fédération de Recherche des Pays de Loire FR9962 of the Centre National de la Recherche Scientifique (CNRS), by the German Research Foundation DFG under grant KL 1105/14/2, and by German Academic Exchange Service DAAD under grant D/0707534. The third author would like to thank the Fraunhofer ITWM for its financial support.

References

[1] A. Ahnesjö, M. Saxner, and A. Trepp, A pencil beam model for photon dose calculation, Med. Phys., 19(2) (1992), 263–273.
[2] P. Andreo, Monte Carlo techniques in medical radiation physics, Phys. Med. Biol., 36(7) (1991), 861–920.
[3] C. Berthon, Stability of the MUSCL schemes for the Euler equations, Commun. Math. Sci., 3 (2005), 133–157.
[4] C. Berthon, Robustness of MUSCL schemes for 2D unstructured meshes, J. Comput. Phys., 218 (2006), 495–509.
[5] C. Berthon, P. Charrier, and B. Dubroca, An HLLC scheme to solve the M1 model of radiative transfer in two space dimensions, J. Sci. Comput., 31 (2007), 347–389.
[6] C. Berthon, J. Dubois, and R. Turpault, Numerical approximation of the M1 model, SMF Publication, Panoramas et Synthèses, 28 (2009), 55–86.
[7] C. Berthon and R. Turpault, Asymptotic preserving HLL schemes, to appear in NMPDE, 2010.
[8] E. Boman, J. Tervo, and M. Vauhkonen, Modelling the transport of ionizing radiation using the finite element method, Phys. Med. Biol., 50 (2005), 265–280.
[9] C. Börgers, Complexity of Monte Carlo and deterministic dose-calculation methods, Phys. Med. Biol., 43 (1998), 517–528.
[10] F. Bouchut, Nonlinear Stability of Finite Volume Methods for Hyperbolic Conservation Laws, and Well-Balanced Schemes for Sources, Frontiers in Mathematics Series, Birkhäuser, 2004.
[11] C. Buet and S. Cordier, An asymptotic preserving scheme for hydrodynamics radiative transfer models: numerics for radiative transfer, Numer. Math., 108 (2007), 199–221.
[12] C. Buet and B. Després, Asymptotic analysis of fluid models for the coupling of radiation and hydrodynamics, J. Quant. Spectrosc. Radiat. Trans., 85 (2004), 385–418.
[13] C. Buet and B. Després, Asymptotic preserving and positive schemes for radiation hydrodynamics, J. Comput. Phys., 215 (2006), 717–740.
[14] J. E. Cygler et al., Clinical use of a commercial monte carlo treatment planning system for electron beams, Phys. Med. Biol., 50 (2005), 1029–1034.
[15] B. Dubroca and J. L. Feugeas, Entropic moment closure hierarchy for the radiative transfer equation, C. R. Acad. Sci. Paris Ser. I., 329 (1999), 915–920.
[16] B. Dubroca and M. Frank, An iterative method for transport equations in radiotherapy, submitted to Proceedings of ECMI 08, 2009.

[17] R. Duclous, B. Dubroca, and M. Frank, Deterministic partial differential equation model for dose calculation in electron radiotherapy, Phys. Med. Biol., 55 (2010), 3843–3857.
[18] L. Eyges, Multiple scattering with energy loss, Phys. Rev., 74 (1948), 1534–1535.
[19] M. Frank, B. Dubroca, and A. Klar, Partial moment entropy approximation to radiative transfer, J. Comput. Phys., 218 (2006), 1–18.
[20] M. Frank, H. Hensel, and A. Klar, A fast and accurate moment method for dose calculation in electron radiotherapy, SIAM J. Appl. Math., 67 (2007), 582–603.
[21] L. Gosse and G. Toscani, Asymptotic-preserving well-balanced scheme for the hyperbolic heat equations, C. R. Math. Acad. Sci. Paris, 334 (2002), 337–342.
[22] L. Gosse and G. Toscani, Space localization and well-balanced schemes for discrete kinetic models in diffusive regimes, SIAM J. Numer. Anal., 41 (2003), 641–658.
[23] T. Goudon, J. F. Coulombel, and F. Golse, Diffusion approximation and entropy-based moment closure for kinetic equations, Asymp. Anal., 45(1-2) (2005), 1–39.
[24] H. Grad, On kinetic theory of rarified gases, Commun. Pure Appl. Math., 2 (1949), 331–407.
[25] A. Harten, P. D. Lax, and B. van Leer, On upstream differencing and Godunov-type schemes for hyperbolic conservation laws, SIAM Rev., 25 (1983), 35–61.
[26] K. R. Hogstrom, M. D. Mills, and P. R. Almond, Electron beam dose calculations, Phys. Med. Biol., 26(3) (1981), 445–459.
[27] D. Jette, Electron dose calculation using multiple-scattering theory, A. Gaussian multiple-scattering theory, Med. Phys., 15(2) (1988), 123–137.
[28] D. Jette and A. Bielajew, Electron dose calculation using multiple-scattering theory: second-order multiple-scattering theory, Med. Phys., 16(5) (1989), 698–711.
[29] T. Krieger and O. A. Sauer, Monte Carlo- versus pencil-beam-/collapsed-cone- dose calculation in a heterogeneous multi-layer phantom, Phys. Med. Biol., 50 (2005), 859–868.
[30] R. J. Kudchadker, J. A. Antolak, W. H. Morrison, P. F. Wong, and K. R. Hogstrom, Utilization of custom electron bolus in head and neck radiotherapy, J. Appl. Clin. Med. Phys., 4 (2003), 321–333.
[31] R. J. LeVeque, Finite Volume Methods for Hyperbolic Problems, Cambridge University Press, 2002.
[32] C. D. Levermore, Moment closure hierarchies for kinetic theories, J. Stat. Phys., 83 (1996), 1021–1065.
[33] D. Mihalas and B. Weibel-Mihalas, Foundations of Radiation Hydrodynamics, Dover, 1999.
[34] G. N. Minerbo, Maximum entropy Eddington factors, J. Quant. Spectrosc. Radiat. Trans., 20 (1978), 541–545.
[35] G. C. Pomraning, The Equations of Radiation Hydrodynamics, Pergamon Press, 1973.
[36] F. Salvat, J. M. Fernandez-Varea, and J. Sempau, PENELOPE-2008, A Code System for Monte Carlo Simulation of Electron and Photon Transport, OECD, 2008, ISBN 978-92-64-99066-1.
[37] A. S. Shiu and K. R. Hogstrom, Pencil-beam redefinition algorithm for electron dose distributions, Med. Phys., 18(1) (1991), 7–18.
[38] C. L. H. Siantar et al., Description and dosimetric verification of the peregrine Monte Carlo dose calculation system for photon beams incident on a water phantom, Med. Phys., 28(7) (2001), 1322–1337.
[39] E. Spezi and G. Lewis, An overview of Monte Carlo treatment planning for radiotherapy, Radiat. Prot. Dos., 131(1) (2008), 123–129.
[40] E. F. Toro, Riemann Solvers and Numerical Methods for Fluid Dynamics, A Practical Introduction, Second edition, Springer-Verlag, Berlin, 1999.
[41] R. Turpault, A consistent multigroup model for radiative transfer and its underlying mean

opacities, J. Quant. Spectrosc. Radiat. Trans., 94 (2005), 357–371.
[42] R. Turpault, M. Frank, B. Dubroca, and A. Klar, Multigroup half space moment approximations to the radiative heat transfer equations, J. Comput. Phys., 198 (2004), 363–371.
[43] B. van Leer, Towards the ultimate conservative difference scheme, V, a second-order sequel to Godunov's method, J. Comput. Phys., 32 (1979), 101–136.
[44] O. N. Vassiliev et al., Feasibility of a multigroup deterministic solution method for 3d radiotherapy dose calculations, Int. J. Radiat. Oncol. Biol. Phys., 72(1) (2008), 220–227.
[45] X. Wen and S. Jin, Convergence of an immersed interface upwind scheme for linear advection equations with piecewise constant coefficients *i*: L_1-error estimates, J. Comput. Math., 26 (2008), 1–22.